Infinite Periodic Boundary Conditions in FEKO

Johann van Tonder and Ulrich Jakobus
EM Software and Systems – S.A. (Pty) Ltd
Stellenbosch, South Africa
jvtonder@emss.co.za , jakobus@emss.co.za

Abstract ─ Infinite periodic boundary conditions (PBC's) implemented in FEKO are presented. To enable the analysis of a wide variety of problems, the PBC includes dielectric objects, metallic surfaces, metallic wires and connection points between wires and surfaces. In addition, the geometry is allowed to touch the periodic boundaries (i.e. continuous current flow onto the neighboring cell which requires special basis function treatment).

Index Terms─ FEKO, Periodic Structures, Antenna Arrays, Frequency Selective Surfaces.

I. INTRODUCTION

FEKO [1] is a commercial and comprehensive 3-D electromagnetic field solver which can be applied to a variety of problems. This paper focuses on periodic structures, for example antenna arrays and frequency selective surfaces. In particular, infinite periodic structures will be analyzed by considering only the unit cell element. Although FEKO can model large finite arrays with the Multilevel Fast Multipole Method (MLFMM), the computational resources of the PBC are much cheaper since we only consider one single unit cell element.

The paper is outlined as follows: Implementation details are given in Section II, verification examples in Sections III-IV, and finally the conclusions in Section V.

II. PERIODIC BOUNDARY CONDITION

The PBC feature enables the analysis of infinite periodic structures by simulating only a single unit cell element. Both 1-D and 2-D (including skewed) lattices are allowed as shown in Figs. 1 and 2, respectively. The phase shift along the lattice vectors can be determined automatically if a plane wave is used as excitation, or it can be specified by the user (say antenna array). Large but finite sized arrays can be approximated as an infinite array. This allows the use of the PBC to minimize the total number of unknowns (and therefore memory) as well as the computation time.
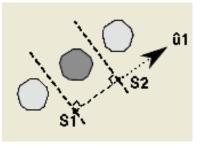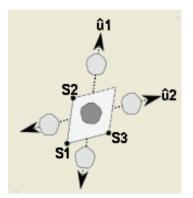

Fig. 1. 1-D periodic boundary.

Fig. 2. 2-D periodic boundary with skewed lattice.

A. Geometry Across Boundary

FEKO allows the geometry to touch the periodic boundary (i.e. one part in one cell will then be connected to another geometry part in the neighboring cell). The two unit cells in Fig. 3 are equivalent (different split of a patch array) and will produce the same results.

Modified Rao-Wilton-Glisson (RWG) [2] basis functions on the boundary in Fig. 4 ensure

continuous current flow across the unit cell boundary into the neighboring periodic element.
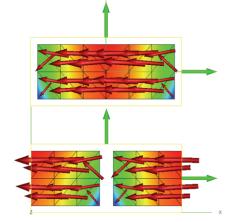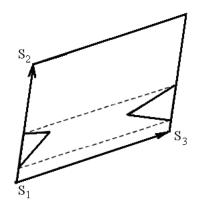

Fig. 3. Current on equivalent unit cells.

Fig. 4. Special basis function on boundaries.

B. Ewald Transformation

The free space 2-D periodic Green's function in the spectral domain has the form [3]

$$G_p(r, r_s) = \sum_{m=-\infty}^{\infty} \sum_{n=-\infty}^{\infty} \frac{e^{-jk_{tmn}\cdot(\rho-\rho_s)}}{2jAk_{zmn}} \cdot [\, e^{-jk_{zmn}|z-z_s|}]$$

(1)

and in the spatial domain [3]

$$G_p(r, r_s) = \sum_{m=-\infty}^{\infty} \sum_{n=-\infty}^{\infty} e^{-jk_{too}\cdot\rho_{mn}} \frac{e^{-jk_0 R_{mn}}}{4\pi R_{mn}}.$$

(2)

For high accuracy, the PBC implementation uses the Ewald transformation in order to get fast convergence for these infinite sums. In this formulation, the periodic Green's function is written as the sum of a modified spectral portion and a modified spatial portion [3]

$$G_p(r, r_s) = G_{p1}(r, r_s) + G_{p2}(r, r_s).$$

(3)

The modified spectral portion contains the complex error function, and is given by [3]

$$G_{p1}(r, r_s) = \sum_{m=-\infty}^{\infty} \sum_{n=-\infty}^{\infty} \frac{e^{-jk_{tmn}\cdot(\rho-\rho_s)}}{4jAk_{zmn}} \cdot [$$
$$\sum_{\pm} e^{\pm jk_{zmn}|z-z_s|} \, \text{erfc}\left(\frac{jk_{zmn}}{2E} \pm |z - z_s| E\right)].$$

(4)

Similarly, the modified spatial portion is [3]

$$G_{p2}(r, r_s) = \sum_{m=-\infty}^{\infty} \sum_{n=-\infty}^{\infty} \frac{e^{-jk_{too}\cdot\rho_{mn}}}{8\pi R_{mn}} \cdot [$$
$$\sum_{\pm} e^{\pm jk_0 R_{mn}} \, \text{erfc}\left(R_{mn}E \pm \frac{jk}{2E}\right)].$$

(5)

The number of terms in the infinite sums is determined automatically by adding more terms until convergence (within 0.01%) is reached. It includes the required Floquet modes (both propagating and evanescent) to achieve high accuracy.

The Ewald transform is also used for the 1-D PBC implementation. The modified spatial portion is the same as for the 2-D case, but the modified spectral portion now contains the exponential integral [4]

$$\frac{1}{4\pi d} \sum_{q=-\infty}^{\infty} e^{-jk_{zq}z} \sum_{p=0}^{\infty} \frac{(-1)^p}{p!} (\rho E)^{2p} E_{p+1}\left(\frac{-k_{\rho q}^2}{4E^2}\right).$$

(6)

C. Dielectrics

In the Method of Moments (MoM), metallic and dielectric triangles allow the use of the surface equivalence principle (SEP) to model any dielectrics within the unit cell. Since we allow the geometry to extend across the unit cell (by using special basis functions), infinite dielectric regions can also be modeled. This makes FEKO a powerful tool to analyze printed antennas with inhomogeneous media. The SEP has a clear advantage over both the finite-element/boundary-integral (FE/BI) method [3], and the hybrid MoM/Green's function method [5] where the volume equivalence principle (VEP) is used. The SEP only meshes the surface of the dielectric, whereas the FE/BI and VEP methods use volume elements to mesh the dielectric.

Another advantage of using the SEP is that we can ignore all dielectric surfaces which are located on the unit cell boundaries. This is valid since identical dielectrics are touching the boundary surface on both the inside and outside (from the neighboring unit cell). In contrast, for the FE/BI method the boundary conditions must also be imposed on the FE mesh located on these side walls.

Multiple dielectric regions are allowed to touch the same boundary to enable the analyses of, for example, a dielectric substrate with periodic holes. The advantages of the SEP will become clear in the microstrip example in the next section.

III. EXAMPLES

A. Pin-fed Microstrip Patch Array

Consider the pin fed microstrip patch antenna in Fig. 5, with side lengths $L = W = 30$ mm and vertical feed probe at $(x,y) = (-7.5,0)$ mm. The unit cell is square with dimensions $a = b = 50$ mm, substrate permittivity $\varepsilon_r = 2.55$ and substrate thickness $d = 2$ mm. A close-up of the pin-fed excitation is shown in Fig. 6, consisting of two wire segments connecting the ground plane and the patch.

The SEP is used to model the dielectric, with the vertical side walls excluded from the mesh below. The ground plane and patch are modeled with metallic triangles, and dielectric triangles are used to model the top dielectric interface. There are special basis functions on the periodic boundaries for both the metallic and dielectric triangles to ensure current continuity.
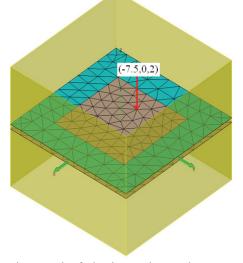

Fig. 5. Pin-fed microstrip patch array.

The active input impedance is defined as the input impedance in the active array environment when all elements are excited. We will compute the active input impedance when all elements are fed in phase to produce a main beam at broadside. The calculated broadside scanning input resistance and reactance are shown in Figs. 7 and 8, respectively. Good agreement to the published FE/BI results [6] can be seen.
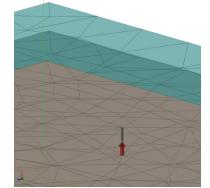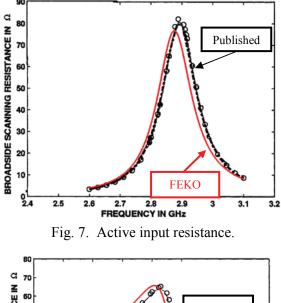

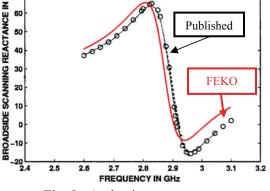Fig. 6. Close-up of pin-fed excitation.

Fig. 7. Active input resistance.

Fig. 8. Active input reactance.

B. Printed Dipole Array

Scan blindness will be demonstrated for the infinite array of printed dipoles [5] in Fig. 9. Parameters: Dipole length $L = 0.39\ \lambda$, width $W = 0.01\ \lambda$, square unit cell $a = b = 0.5\ \lambda$, substrate thickness $d = 0.19\ \lambda$ and permittivity $\varepsilon_r = 2.55$. The centre of the dipole is excited by an edge voltage source.

The active reflection coefficient is defined when all dipoles are excited with the correct phase to produce a main beam in the direction ϑ ($\vartheta = 0°$ is broadside):

$$R(\vartheta) = \frac{Z_{in}(\vartheta) - Z_{in}(\vartheta = 0°)}{Z_{in}(\vartheta) + Z_{in}^*(\vartheta = 0°)}. \tag{7}$$

The feed network is matched for broadside scanning to the internal source impedance of $Z_{in}\ (\vartheta = 0°)$.

The computed active reflection coefficient versus scan angle compares very well to the published results [5], for both magnitude and phase as shown in Figs. 10 and 11, respectively. Note the unity reflection coefficient at the scan blindness angle of $45°$.
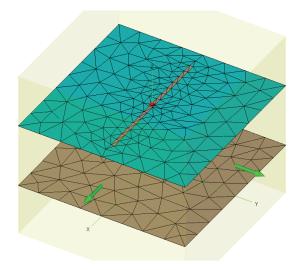

Fig. 9. Printed dipole array.

C. Frequency Selective Surfaces

The Jerusalem-cross frequency selective surface (FSS) in Fig. 12 was analyzed. Fig. 13 shows the unit cell and plane wave excitation.
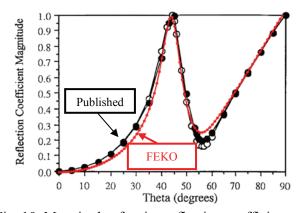

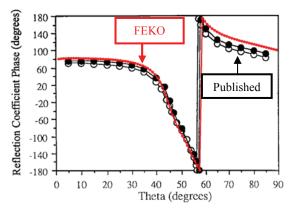Fig. 10. Magnitude of active reflection coefficient.

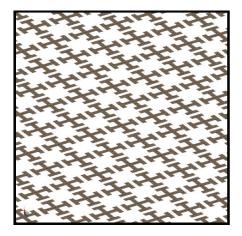Fig. 11. Phase of active reflection coefficient.

Fig. 12. Jerusalem-cross FSS.

To verify the PBC results the MLFMM was used to analyze a large finite 51x51 FSS. Excellent agreement in the current distribution at 7 GHz can be seen in Figs. 14 and 15.
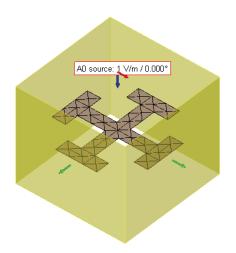
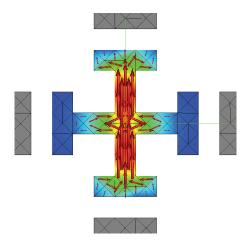Fig. 13. FSS unit cell and plane wave excitation.

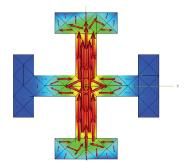Fig. 14. Finite 51x51 FSS solved with MLFMM.

Fig. 15. Single element solved with infinite PBC.

The magnitude and phase of the reflection coefficient (versus frequency) are plotted in Figs. 16 and 17, respectively. This is for a normal incident plane wave on the FSS. Excellent agreement to the published results [7] can be seen, for both magnitude and phase.
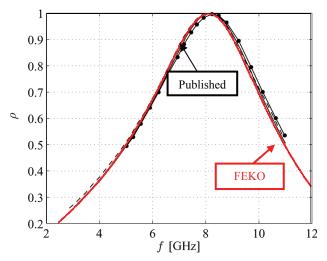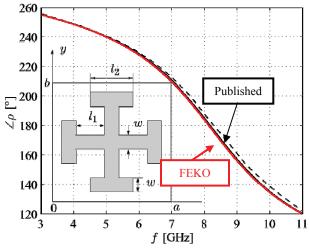

Fig. 16. Magnitude of the reflection coefficient.

Fig. 17. Phase of the reflection coefficient.

D. Infinite Cylinder

An infinite cylinder shown in Fig. 18 is modeled as a finite cylinder with 1-D PBC at both ends. FEKO can handle arbitrary incidence, but the published results for this example used a *z*-directed normal incident plane wave. The diameter of the cylinder is varied and the scattered electric field is computed versus the observation angle, in order to get the scattering width (SW) defined as

$$\sigma_{2-D} = \lim_{\rho \to \infty} \left(2\pi\rho \, \frac{|E_z^s|^2}{|E_z^i|^2} \right).$$

(8)

In Fig. 19 the computed SW is in very good agreement to the published results [8].
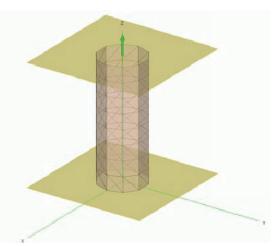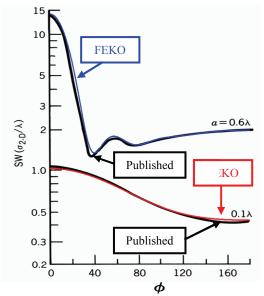
Fig. 18. Unit cell of infinite cylinder.

Fig. 19. Scattering width of infinite cylinder.

E. Infinite Wire

To verify the implementation of the special basis functions for wires at 1-D periodic boundaries consider the infinite z-directed wire, with the unit cell shown in Fig. 20. A z-directed plane wave is incident along the x-axis. The near-field for the infinite wire is known analytically [8]. The computed near electric and magnetic fields are shown in Figs. 21 and 22, respectively. Excellent agreement to the analytical values can be seen. This verifies the special basis function implementation for wires at the boundaries, as well as the near-field computation for both electric and magnetic fields together with the PBC.
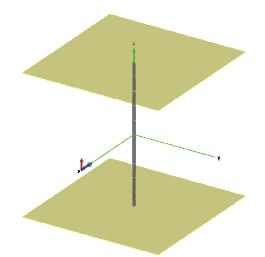

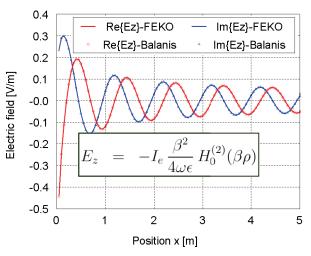Fig. 20. Unit cell of infinite wire.

$$E_z = -I_e \frac{\beta^2}{4\omega\epsilon} H_0^{(2)}(\beta\rho)$$

Fig. 21. Near electric field of infinite wire.

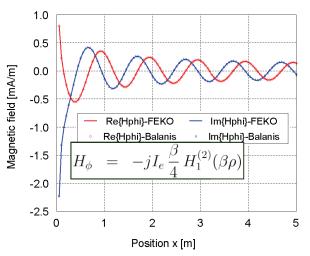$$H_\phi = -jI_e \frac{\beta}{4} H_1^{(2)}(\beta\rho)$$

Fig. 22. Near magnetic field of infinite wire.

IV. FAR-FIELD

In this section the far-field of a finite MxN array will be computed using the infinite array approximation to obtain the current distribution on the elements. Consider the example of a 2-D antenna array of strip dipoles, with the unit cell in Fig. 23. Parameters: Dipole length $L = 0.45$ λ, width $W = 0.02$ λ, unit cell length $a = 0.50$ λ and width $b = 0.30$ λ. The elements are fed with the correct phase increment to obtain a main beam pointing in the direction ϑ=20°, requiring a phase increment of $(2\pi a/\lambda)\sin\vartheta= 61.564°$.
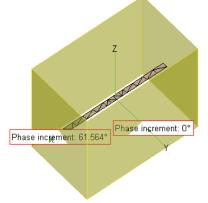

Fig. 23. Unit cell of strip dipole array.

The PBC analysis will give the correct current distribution on the unit cell dipole in an infinite array environment (including all mutual coupling). With this current distribution, the single unit cell dipole on its own radiates a doughnut shaped far-field pattern as shown in Fig. 24.
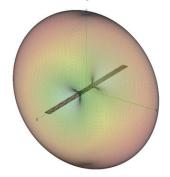

Fig. 24. Far-field of single unit cell element.

To compute the far-field of a finite MxN array as shown in Fig. 25, we sum the far-field pattern of the unit cell with the correct phase and position of each element in the array. Computing the far-field using the PBC ignores edge effects, since it assumes that the current distribution is identical on

all array elements (except for the phase shift). The far-field computed with the PBC approximation was validated using the MLFMM, which analyzes the complete finite array. The MLFMM computes the correct currents on all elements and includes edge effects. Results for two array sizes are shown in Figs. 26 and 27. As expected, the main beam points in the direction ϑ=20°. Good agreement between the PBC approximation and the MLFMM can be seen.
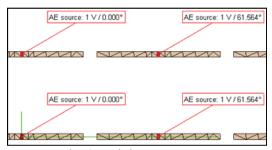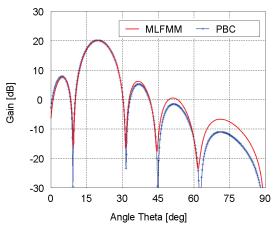

Fig. 25. Finite MxN array.

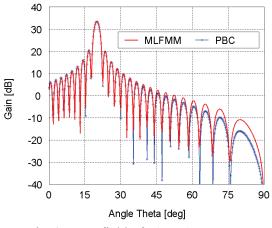Fig. 26. Far-field of 11 x 11 array.

Fig. 27. Far-field of 51 x 51 array.

V. CONCLUSIONS

Infinite periodic boundary conditions were implemented in FEKO using the efficient Ewald transform to obtain fast convergence for the infinite sums. Both 1-D and 2-D (including skewed) lattices are supported. The geometry is allowed to extend into the neighboring cell with the use of special basis functions on the boundary. The phase shift along the periodic lattice can be determined automatically from plane wave excitations, or it can be specified by the user. The PBC includes metallic and dielectric triangles, wires, connection points. This makes FEKO a powerful tool to analyze printed antenna arrays with inhomogeneous media and also frequency selective surfaces. By ignoring edge effects, the PBC enables efficient far-field calculations of finite *M*x*N* arrays.

REFERENCES

[1] EM Software and Systems – S.A. (Pty) Ltd, Stellenbosch, South Africa: *FEKO – Field Computations Involving Bodies of Arbitrary Shape*, http://www.feko.info.

[2] S. M. Rao, D. R. Wilton and A. W. Glisson, "Electromagnetic Scattering by Surfaces of Arbitrary Shape*", IEEE Trans. Antennas Propagat.*, vol. 30, no. 3, pp. 409-418, May 1982.

[3] T. F. Eibert, J. L. Volakis, D. R. Wilton and D. R. Jackson, "Hybrid FE/BI Modeling of 3-D Doubly Periodic Structures Utilizing Triangular Prismatic Elements and an MPIE Formulation Accelerated by the Ewald Transformation*", IEEE Trans. Antennas Propagat.*, vol. 47, no. 5, pp. 843-849, May 1999.

[4] F. Capolino, D. R. Wilton and W. A. Johnson, "Efficient computation of the 3D Green's function for the Helmholtz operator for a linear array of point sources using the Ewald method", *Journal of Computational Physics*, vol. 223, pp. 250-261, 2007.

[5] W. J. Tsay and D. M. Pozar, "Radiation and Scattering from Infinite Periodic Printed Antennas with Inhomogeneous Media", *IEEE Trans. Antennas Propagat.*, vol. 46, no. 11, pp. 1641-1650, 1998.

[6] D. S. Filipovic, L. S. Anderson and J. L. Volakis, "A Multiresolution Method for Simulating Infinite Periodic Arrays", *IEEE Trans. Antennas Propagat.*, vol. 48, no. 11, pp. 1784-1786, November 2000.

[7] I. Stevanovic, P. Crespo-Valero, K. Blagovic, F. Bongard and J. R. Mosig, "Integral-Equation Analysis of 3-D Metallic Objects Arranged in 2-D Lattices Using the Ewald Transformation", *IEEE Trans. Microwave Theory and Techniques*, vol. 54, no. 10, pp. 3688-3697, October 2006.

[8] C. A. Balanis, Advanced Engineering Electromagnetics, Wiley, pp. 607, 1989.

Johann van Tonder received the Ph.D. degree in electronic engineering from the University of Stellenbosch, South Africa, in 1995. Since 1996, he has been a FEKO research and development engineer.

Ulrich Jakobus received the diploma, doctoral, and Habilitation degrees in Electrical Engineering from the University of Stuttgart, Germany in 1991, 1994, and 1999, respectively. The focus of his research was numerical algorithms for high frequency electromagnetic simulations and the development of the computer code FEKO. In October 2000 he joined EM Software & Systems, Stellenbosch, South Africa, where he is a Director, the FEKO Product Manager, and heading the FEKO kernel team.